THERMAL IMAGING AND ANALYSIS OF CARBON NANOTUBE COMPOSITES

BY

FEIFEI LIAN

THESIS

Submitted in partial fulfillment of the requirements
for the degree of Master of Science in Electrical and Computer Engineering
in the Graduate College of the
University of Illinois at Urbana-Champaign, 2013

Urbana, Illinois

Adviser:

Associate Professor Eric Pop

Abstract

Carbon nanotube (CNT) films have a broad range of applications, from solar cells and transistors to bolometers and mechanical reinforcement additives for polymers. However, surprisingly little is still known about the thermal properties of such CNT films, and in particular about the intertube junctions. This study examines suspended films of conductive single-wall CNT (SWNT) films through electrical measurements and optical infrared (IR) thermometry in order to simultaneously characterize their electrical and thermal properties. Using an IR microscope, the real-time temperature profile of such CNT films under bias is mapped and used to extract thermal conductivity. A computation model was also developed to fit the one-dimensional heat diffusion equation to the temperature profile captured by the IR scope, including the effect of thermal contact resistance and heat loss to ambient. Transfer length method measurements were used to extract electrical contact resistance between the film and the electrodes. These methods were applied to investigate the properties of CNT films with several different morphologies, revealing that both electrical and thermal properties are strongly dependent on CNT volume density and junction within the films. Understanding fundamental transport within CNT networks allows us to try and decouple the properties and engineer novel materials for applications such as energy harvesting using thermoelectric power generation.

Acknowledgments

I would like to thank my advisor, Professor Eric Pop, for his guidance through my undergraduate and graduate studies at the University of Illinois. I am very grateful for the opportunity to work with you and the Pop group. I would like to thank Dr. David Estrada for his mentorship. Your advice on research, graduate school, and life in general has been invaluable. I would like to thank my fellow group members Zuanyi Li, Sharnali Islam, Vincent Dorgan, Juan Pablo Llinas, Alicia Hoag, and Josh Wood. Our discussions are always intellectually stimulating as well as entertaining. I would like to acknowledge my collaborators Professor Esko Kauppinen, Professor Sanjiv Sinha, Professor Satish Kumar, Dr. Albert Nasibulin, Dr. Brent Walling, Hongxiang Tian, and Man Prakash Gupta. I would like to thank the staff of the Micro and Nanotechnology Laboratory for their help and technical support. I would like to thank Alex Province for all your love and support. Finally, I would like to thank my parents for believing in me and pushing me to dream big.

Table of Contents

1. Introduction

1.1 Waste Heat Energy Recovery

Approximately two-thirds of the energy consumed for electricity generation is rejected in the form of waste heat during conversion [1]. One of the ways to convert heat directly to electricity is through the use of thermoelectric (TE) power generation [2, 3]. TE materials have an electrical potential in the presence of a thermal gradient that can be directly related to a property call the Seebeck effect. The Seebeck coefficient of a material is given by the open circuit voltage divided by the temperature difference across the material [1]:

$$S = -\frac{\Delta V}{\Delta T} \tag{1.1}$$

Since the Seebeck coefficient alone does not guarantee high power generation, the quality of a TE material performance is characterized by its figure of merit [1]:

$$ZT = \frac{S^2 \sigma}{\kappa} T \tag{1.2}$$

where S is the Seebeck coefficient, σ is the electrical conductivity, κ is the thermal conductivity, and T is the temperature. From the figure of merit, we can see that an ideal TE material has a high Seebeck coefficient, a high electrical conductivity, and a low thermal conductivity. Figure 1.1 shows the current efficiencies offered by TEs in comparison with mechanical heat engines [4]. TE performance is not yet comparable with mechanical heat engines.

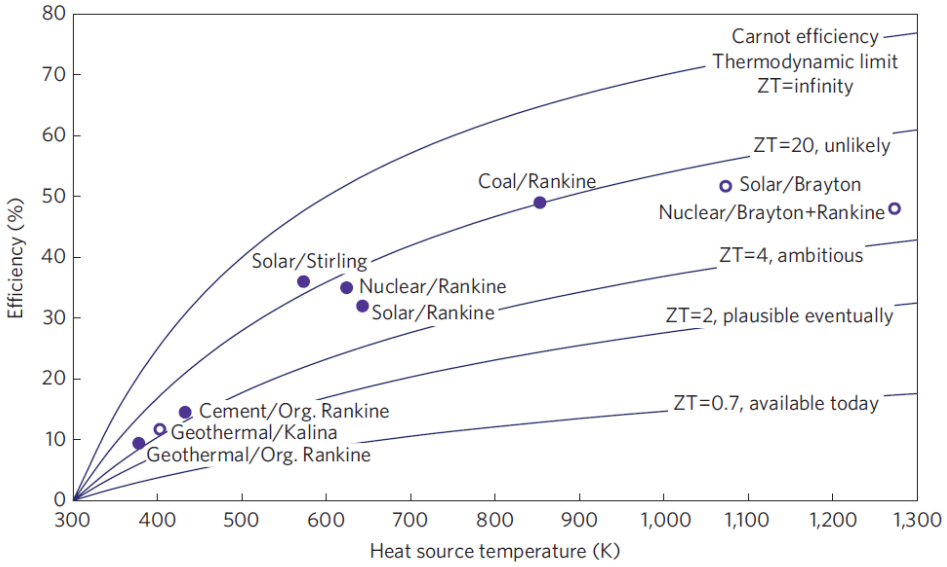

Figure 1.1: Comparison of thermoelectric efficiency with various heat engines [4].

There are several issues that have stood in the way of the mass production and widespread integration of TEs for waste heat recovery. Top performing TE materials such as bismuth telluride (Bi_2Te_3) can cost as much as $7/W [5]. Engineers must reduce the cost per watt of TE generators to make them an attractive option for waste heat recovery. Efficiency is another main issue with TE generators. Ultimately, the goal of engineers is to achieve ZT = 3 for thermoelectric materials [4].

Nanotechnology allows for phonon engineering to improve the TE figure of merit in materials [2]. We can use confinement to decrease the thermal conductivity of materials since the phonon mean free path is much less than the electron mean free path. This means that if we reduce the size of a material, the phonon will scatter before the electron will scatter [6, 7]. This results in a thermal conductivity reduction without affecting the electrical conductivity. Two groups demonstrated this concept using silicon nanowires that were smooth and etched on the surface [8, 9].

In order to address the cost of TE materials, we can consider other more abundant semiconductors such as carbon-based materials [5]. One problem with carbon nanomaterials is that the thermal conductivity of some allotropes of carbon is high, an undesirable property for TEs [10]. Previous works have demonstrated methods of modifying the thermal conductivity in carbon materials [11-16]. In this work, we study the fundamental thermal transport in carbon nanotube films and develop a method of rapid analysis of conductive bulk films. We seek to understand the fundamental transport in order to engineer materials for thermoelectric applications.

1.2 Thermal Conductivity in Carbon Nanotube Networks

Carbon-based nanomaterials have a wide range of thermal conductivities due to the various allotropes and their atomic structures. In sp^2 and sp^3 hybridized carbon lattices, thermal conductivities can exceed 3000 $Wm^{-1}K^{-1}$, whereas amorphous carbon can have $\kappa \sim$ 0.01 $Wm^{-1}K^{-1}$ (Figure 1.2) [10]. An atomic layer of sp^2 bonded carbon arranged in a hexagonal lattice is called graphene. A carbon nanotube (CNT) is a sheet of graphene rolled into a cylinder as shown in Figure 1.3a. Carbon nanotubes can be either semiconducting or metallic depending on the chirality of the tube [17]. In a random network of CNTs, approximately two-thirds of the CNTs have semiconducting properties and one-third have metallic properties (Figure 1.3b) [17].

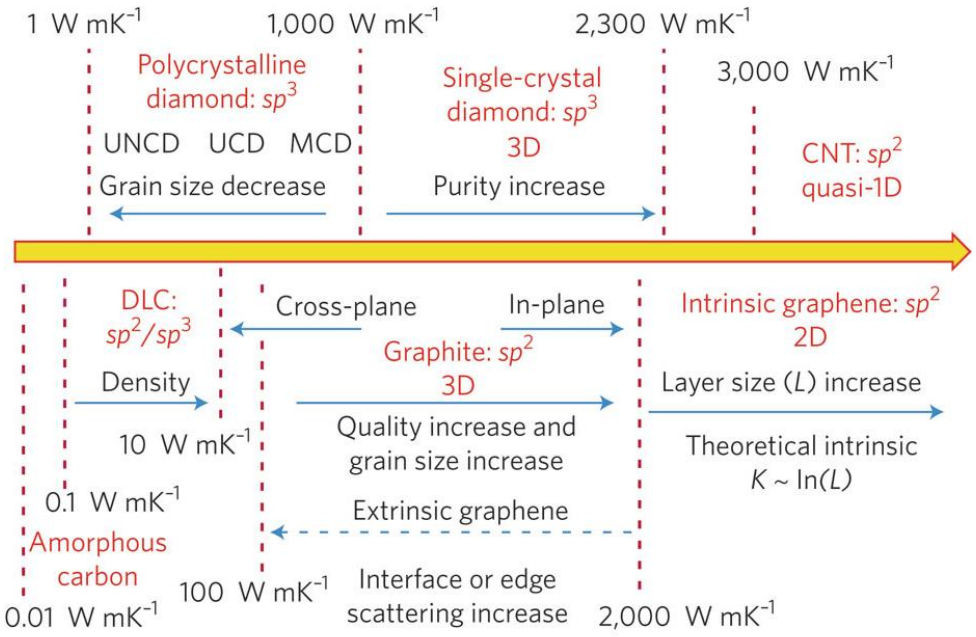

Figure 1.2: Thermal conductivity of various allotropes of carbon. Amorphous carbon has very low thermal conductivity, whereas CNTs have extremely high thermal conductivity [10].

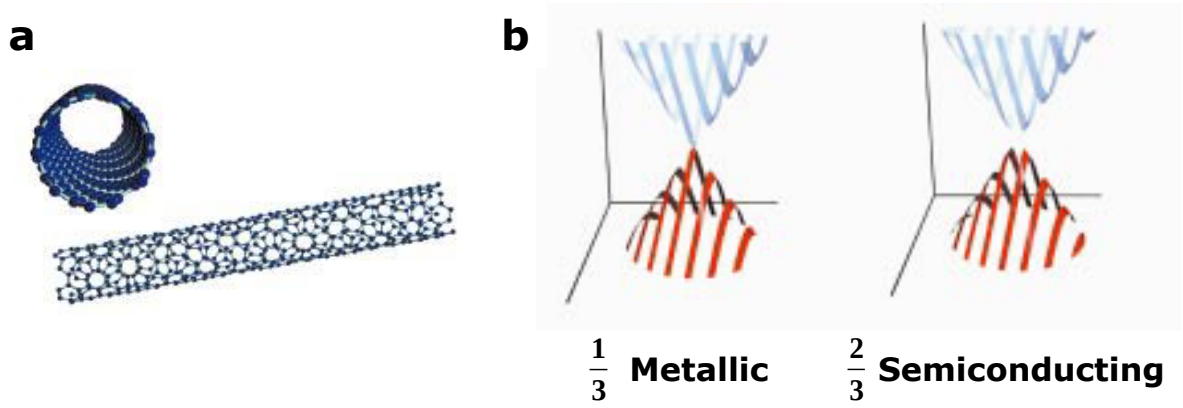

Figure 1.3: (a) Single-walled carbon nanotube [17]. **(b)** Energy dispersion relation for semiconducting and metallic SWNTs. Semiconducting nanotubes have a band gap and make up approximately two-thirds of a network of random SWNTs. Metallic CNTs have no band gap and make up the other one-third of the network [17].

In CNT networks and films, the effective thermal conductivity of the network is much lower than the thermal conductivity of individual CNTs. This is due to the high inter-tube junction thermal resistance [11, 18, 19]. Previous studies on thermal conductivity in CNT networks have found κ to reduce by almost 3 orders of magnitude depending on the CNT junction density in the network [11]. Prasher et al. estimated the thermal conductivity of dense beds of SWNTs to be a function of the volume fraction ϕ:

$$\kappa_{\text{bed}} = 1/3\kappa_{\text{CNT}}\phi \tag{1.3}$$

Volume fraction can be altered by mechanical pressure or by using solvents to densify the network [11, 20]. Figure 1.4 shows thermal conductivities of individual CNTs and CNT networks.

Previous work shows that electrical conductivity scales as a function of the average nanotube bundle length, $L_{\text{av}}^{1.46}$, since longer tubes will have fewer junctions in order to cross a surface [21]. Hecht et al. also predicts that the electrical conductivity of a network of CNTs should scale with the CNT bundle diameter as a function of $1/D_{av}^{\beta}$, where D_{av} is the average diameter of the nanotube bundle and β describes the rigidity of the SWNT bundle [21]. For thermal conductivity scaling with nanotube morphology, Volkov et al. explored the thermal transport of networks and the effect of nanotube density and average length using a combination of theoretical analysis and mesoscopic simulations [22]. Assuming that nanotube chirality is the same throughout the network and the mass density is 0.2 gcm^{-1}, the thermal conductivity scales as $\kappa \sim L^2$ for 3D bulk films and for quasi 2D films where L is the nanotube length. Zhong and Lukes have shown through molecular dynamics simulations that the thermal interfacial resistance of CNT junctions decreases as nanotube overlap area increases [19]. Finally, although previous works have shown that junction type, e.g. between

metallic (M) and semiconducting (S) CNTs, affect electrical transport, no study has explored the thermal transport in networks with controlled junction type, bundle diameter, and bundle length [18, 23].

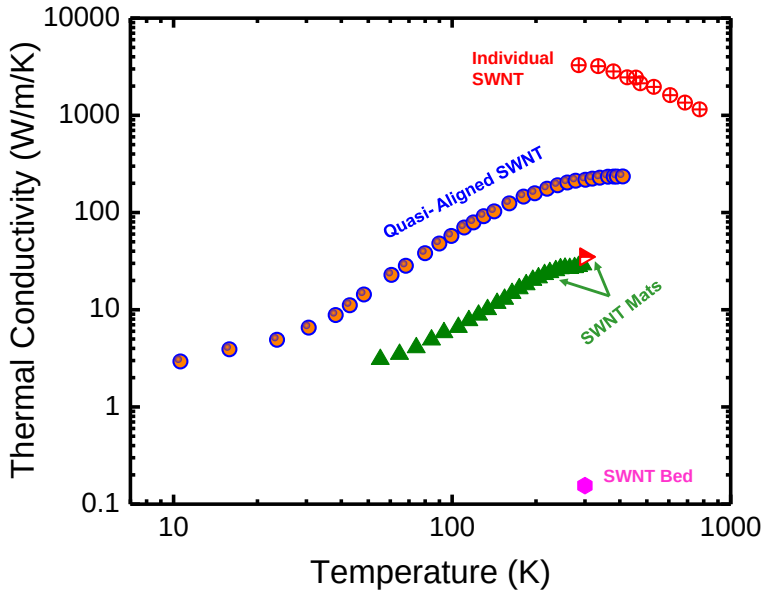

Figure 1.4: Thermal conductivity of an individual SWNT [24], aligned SWNTs [13], SWNT mats (35 nm thick for green triangles [15], mm-scale for red triangle [14]), and SWNT beds (200-800 μm thick) [11].

In order to study the role of CNT network morphology on thermal transport, we must employ a measurement technique to measure the thermal conductivity.

1.3 Thermal Conductivity Measurement Techniques for Low-Dimensional Materials

There are many methods of measuring thermal conductivity of low-dimensional materials. Depending on the material, each technique has its challenges for both

measurement accuracy and difficulty. This section will explore some common thermal conductivity measurement techniques.

1.3.1 Electrical Measurement Techniques

The two main electrical thermometry techniques used for measuring thermal conductivity are the 3ω method and steady-state thermometry technique [25]. Both methods use lithography to pattern metal heaters and thermometers in bridge patterns above the sample. In the 3ω method, the metal line is pulsed with a current at an angular frequency ω [26]. This induces a heating rate and temperature that corresponds to 2ω frequency. The amplitude and phase of the temperature can be extracted from the 3ω voltage that is along the metal line. The 3ω method can be used for both cross-plane and in-plane measurements (Figure 1.5a). In order to do this measurement, the sample must be coated with an insulating dielectric that is continuous. Also, the thickness of the sample must be at least five times greater than the width of the metal line. The 3ω method is difficult to use with CNT films since the surface roughness of the film is very high, making it difficult to deposit a continuous dielectric for insulation.

Steady-state electrical thermometry measures the temperature change by relating the change in resistance of the thermometer line to a change in temperature (Figure 1.5b) [25]. Generally, steady-state electrical thermometry is used to measure the in-plane thermal conductivity of samples. However, similar to the 3ω method, this technique also requires a dielectric to insulate the metal lines from the sample.

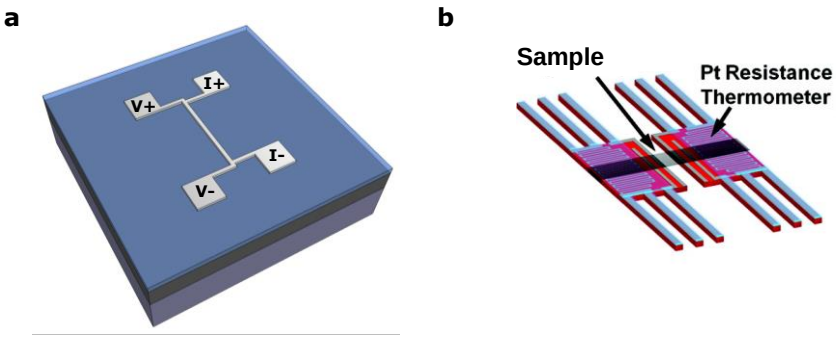

Figure 1.5: (a) 3 omega metal heater line design for cross-plane measurements. Heater line is placed on top of an oxide which is on the sample. **(b)** Steady-state thermometry setup. Sample can be suspended across two heater/thermometer platforms [27].

1.3.2 Raman Thermometry Technique

Raman thermometry is an optical technique that requires very little sample preparation aside from suspension as shown in Figure 1.6 [10]. The main criterion for using Raman thermometry is that the sample must have Raman active modes. First, the material is calibrated by measuring the Raman spectrum as a function of temperature. This gives a peak shift with temperature. Next, the laser is used to heat the sample by increasing laser power to create a temperature change. A detector is placed under the sample to measure the power absorbed by the sample. Once the change in power and corresponding change in temperature is known along with the sample geometry, the thermal conductivity can be extracted from the heat diffusion equation.

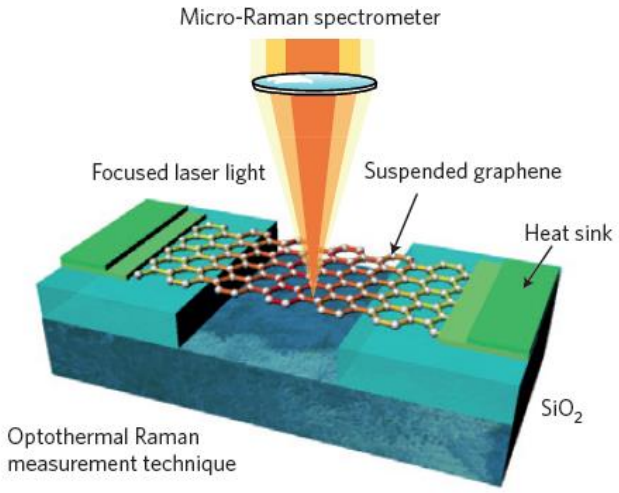

Figure 1.6: Experimental setup for Raman optical thermometry. The sample must be suspended and have Raman active modes [10].

In this thesis, we introduce using infrared thermometry for rapid analysis using suspended infrared imaging coupled with a computational model. We utilize our technique to study the thermal conductivity of CNT networks with varied morphology.

1.4 References

[1] A. Shakouri, "Recent developments in semiconductor thermoelectric physics and materials," *Annual Review of Materials Research,* vol. 41, pp. 399-431, 2011.

[2] G. J. Snyder and E. S. Toberer, "Complex thermoelectric materials," *Nature Materials,* vol. 7, pp. 105-114, 2008.

[3] R. David, "Thermoelectric harvesting of low-temperature heat," in *Modules, Systems, and Applications in Thermoelectrics*, CRC Press, 2012, pp. 1-21.

[4] C. B. Vining, "An inconvenient truth about thermoelectrics," *Nature Materials,* vol. 8, pp. 83-85, 2009.

[5] C. A. Hewitt, A. B. Kaiser, S. Roth, M. Craps, R. Czerw, and D. L. Carroll, "Multilayered carbon nanotube/polymer composite based thermoelectric fabrics," *Nano Letters,* vol. 12, pp. 1307-1310, 2012.

[6] A. Majumdar, "Thermoelectricity in semiconductor nanostructures," *Science,* vol. 303, pp. 777-778, 2004.

[7] J. K. Yu, S. Mitrovic, D. Tham, J. Varghese, and J. R. Heath, "Reduction of thermal conductivity in phononic nanomesh structures," *Nature Nanotechnology,* vol. 5, pp. 718-721, 2010.

[8] A. I. Boukai, Y. Bunimovich, J. Tahir-Kheli, J. K. Yu, W. A. Goddard, and J. R. Heath, "Silicon nanowires as efficient thermoelectric materials," *Nature,* vol. 451, pp. 168-171, 2008.

[9] A. I. Hochbaum, R. K. Chen, R. D. Delgado, W. J. Liang, E. C. Garnett, M. Najarian, et al., "Enhanced thermoelectric performance of rough silicon nanowires," *Nature,* vol. 451, pp. 163-U5, 2008.

[10] A. A. Balandin, "Thermal properties of graphene and nanostructured carbon materials," *Nature Materials,* vol. 10, pp. 569-581, 2011.

[11] R. S. Prasher, X. J. Hu, Y. Chalopin, N. Mingo, K. Lofgreen, S. Volz, et al., "Turning carbon nanotubes from exceptional heat conductors into insulators," *Physical Review Letters,* vol. 102, p. 105901, 2009.

[12] J. Hone, M. C. Llaguno, M. J. Biercuk, A. T. Johnson, B. Batlogg, Z. Benes, et al., "Thermal properties of carbon nanotubes and nanotube-based materials," *Applied Physics A,* vol. 74, pp. 339-343, 2002.

[13] J. Hone, M. C. Llaguno, N. M. Nemes, A. T. Johnson, J. E. Fischer, D. A. Walters, et al., "Electrical and thermal transport properties of magnetically aligned single wall carbon nanotube films," *Applied Physics Letters,* vol. 77, pp. 666-668, 2000.

[14] J. Hone, M. Whitney, C. Piskoti, and A. Zettl, "Thermal conductivity of single-walled carbon nanotubes," *Physical Review B,* vol. 59, pp. 2514-2516, 1999.

[15] M. E. Itkis, F. Borondics, A. Yu, and R. C. Haddon, "Thermal conductivity measurements of semitransparent single-walled carbon nanotube films by a bolometric technique," *Nano Letters,* vol. 7, pp. 900-904, 2007.

[16] N. Xiao, X. C. Dong, L. Song, D. Y. Liu, Y. Tay, S. X. Wu, et al., "Enhanced thermopower of graphene films with oxygen plasma treatment," *ACS Nano,* vol. 5, pp. 2749-2755, 2011.

[17] P. G. Collins and P. Avouris, "Nanotubes for electronics," *Scientific American,* vol. 283, pp. 62-69, 2000.

[18] A. Behnam, V. K. Sangwan, X. Zhong, F. Lian, D. Estrada, D. Jariwala, et al., "High-field transport and thermal reliability of sorted carbon nanotube network devices," *ACS Nano,* vol. 7, pp. 482-490, 2013.

[19] H. Zhong and J. R. Lukes, "Interfacial thermal resistance between carbon nanotubes: Molecular dynamics simulations and analytical thermal modeling," *Physical Review B,* vol. 74, p. 125403, 2006.

[20] A. Kaskela, A. G. Nasibulin, M. Y. Timmermans, B. Aitchison, A. Papadimitratos, Y. Tian, et al., "Aerosol-synthesized SWCNT networks with tunable conductivity and transparency by a dry transfer technique," *Nano Letters,* vol. 10, pp. 4349-4355, 2010.

[21] D. Hecht, L. B. Hu, and G. Gruner, "Conductivity scaling with bundle length and diameter in single walled carbon nanotube networks," *Applied Physics Letters,* vol. 89, 2006.

[22] A. N. Volkov and L. V. Zhigilei, "Scaling laws and mesoscopic modeling of thermal conductivity in carbon nanotube materials," *Physical Review Letters,* vol. 104, p. 215902, 2010.

[23] M. S. Fuhrer, J. Nygard, L. Shih, M. Forero, Y. G. Yoon, M. S. C. Mazzoni, et al., "Crossed nanotube junctions," *Science,* vol. 288, pp. 494-497, 2000.

[24] E. Pop, D. Mann, Q. Wang, K. Goodson, and H. Dai, "Thermal conductance of an individual single-wall carbon nanotube above room temperature," *Nano Letters,* vol. 6, pp. 96-100, 2005.

[25] D. G. Cahill, K. E. Goodson, and A. Majumdar, "Thermometry and thermal transport in micro/nanoscale solid-state devices and structures," *Journal of Heat Transfer,* vol. 124, pp. 223-241, 2002.

[26] D. G. Cahill, "Thermal conductivity measurement from 30 to 750 k: The 3 omega method," *Review of Scientific Instruments,* vol. 61, pp. 802-808, 1990.

[27] M. T. Pettes, I. S. Jo, Z. Yao, and L. Shi, "Influence of polymeric residue on the thermal conductivity of suspended bilayer graphene," *Nano Letters,* vol. 11, pp. 1195-1200, 2011.

2. Experimental Procedures

2.1 Design of Thermometry Platform

To use the Quantum Focus Instruments InfraScope to measure the temperature of the CNT films, we designed a platform that allows for one-dimensional (1D) heat flow across the sample. Heat conduction across the sample is confined to 1D through suspension which eliminates any heat flow into a substrate. Heat flow due to convection and radiation are accounted for in our analytical model, which is discussed in detail in Chapter 3. Our analysis predicts approximately that heat loss through convection and radiation is ~10% since the sample is suspended which results in a higher surface area for heat to escape. The contacts, which must be electrically conductive, must also be large enough to thermally anchor the device so the boundary conditions are isothermal at the edge of the contacts.

Due to the size of the film and the method of transfer, we needed contacts that would physically support the CNT film. We used a design in which the contacts had sufficient surface area for the film to stay anchored [1]. Instead of aluminum for contacts, we used copper (Cu) as a contact metal due to its high thermal and electrical conductivity. The Cu contact dimensions were 4 mm by 4 mm by 20 mm. The contacts were electrically isolated using ceramic washers. The gap length of the suspended region of the film could be increased through the use of additional ceramic washers. To improve electrical contact resistance between the sample and contacts, we polished the Cu contacts and coated the surface with a titanium (Ti) and Pd layer. The Ti layer acted as a sticking layer to help the Pd adhere to the contact surface. Pd has a metal work function that creates an ohmic contact with the CNTs [2, 3].

2.2 Sample Preparation

2.2.1 Carbon Nanotube Growth and Film Fabrication

The CNTs films used in this study came from three different types of CNT synthesis and two types of film transfer. We utilized CNTs synthesized through aerosol chemical vapor deposition (CVD), high pressure carbon monoxide (HiPco), and arc discharge method. The three different growth methods all produce single-walled carbon nanotubes (SWNTs). However, growth processes often result in the formation of catalyst particles along with SWNTs. We compare the three different films to see the effect of different growth methods as well as processing on thermal properties of the networks. Finally, we intended to study the effect of the CNT junction type on thermal properties.

Aerosol CVD is unique in that SWNTs can be grown and deposited onto any substrate due to the fabrication process. The CVD chamber is vertical and the catalyst particles consist of a ferrocene vapor. During growth, the catalyst decomposes in a carbon monoxide atmosphere. Growth of the SWNTs occurs at approximately 880 °C [4, 5]. SWNTs are collected directly on a nitrocellulose filter . Since the SWNTs can be collected directly onto a filter, the SWNT films can be transferred onto a substrate using a dry press transfer method [5]. Figure 2.1a is of a TEM image of the SWNTs grown using the aerosol CVD method, and Figure 2.1b is of the SWNTs on a filter post growth [6]. Aerosol CVD SWNT samples used in our work were provided to us by the NanoMaterials group led by Professor Esko Kauppinen at Aalto University in Finland.

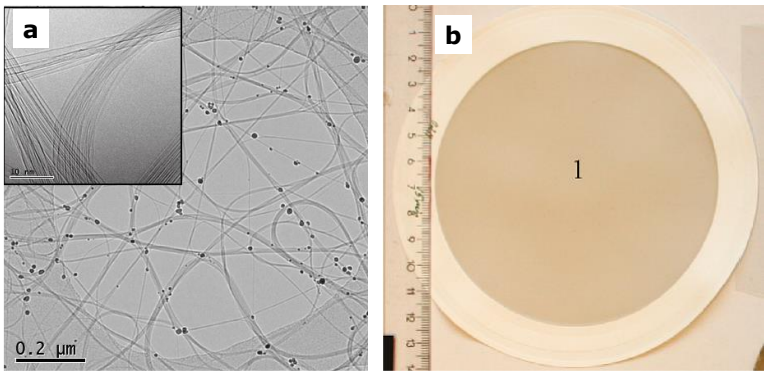

Figure 2.1: (a) TEM image of SWNTs synthesized using the aerosol CVD method. The opaque black spots are the catalyst particles left over from the growth process [6]. **(b)** SWNTs on a nitrocellulose filter [6].

Another method that is commonly used for mass production of SWNTs is through a CVD process called HiPco. In the HiPco process, carbon monoxide (CO) is flowed at high pressure and high temperature into a CVD chamber [7]. SWNTs grow from iron catalyst particles that form *in situ* from iron pentacarbonyl ($Fe(CO)_5$) decomposition and condensation in the CO gas. The HiPco process grows high concentrations of SWNTs and is an attractive method of growing large quantities of SWNTs. Figure 2.2 is of a TEM image of SWNTs with large catalyst particles left over from growth. For our study, we ordered HiPco grown SWNT powder from NanoIntegris.

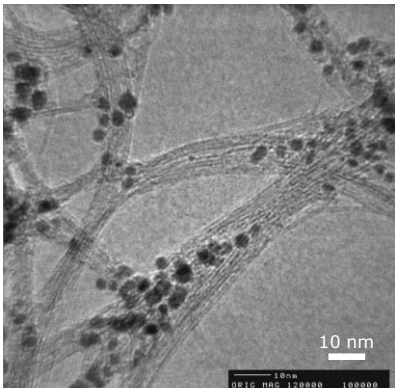

Figure 2.2: TEM image of SWNTs grown using HiPco process. Large catalyst particles can be seen in the nanotube bundles [7].

The third type of CNTs we studied are grown using arc discharge and sorted using density gradient ultracentrifugation (DGU) [8, 9]. Arc discharge CNT synthesis involves applying an electrical potential of ~18 V between two graphite rods that are different diameters. A plasma forms when the graphitic rods are brought together in an inert gas atmosphere and a discharge occurs. This discharge results in the smaller rod being consumed and a deposit of carbon nanotubes on the larger rod. Figure 2.3a is a TEM image of CNTs synthesized through arc discharge [8]. This method of growth can produce multi-walled or single-walled CNTs depending on the concentration of helium gas the discharge takes place in. To separate the semiconducting SWNTs from the metallic SWNTs, Professor Hersam's group at Northwestern University developed a DGU separation technique [9]. SWNTs are dispersed in a surfactant using a horn sonicator. Due to the surfactant encapsulation around the SWNTs, centrifugation can be used to separate SWNTs by diameter, band gap, or electronic type as shown in Figure 2.3b. For our measurements, we purchased sorted SWNTs in solution from NanoIntegris.

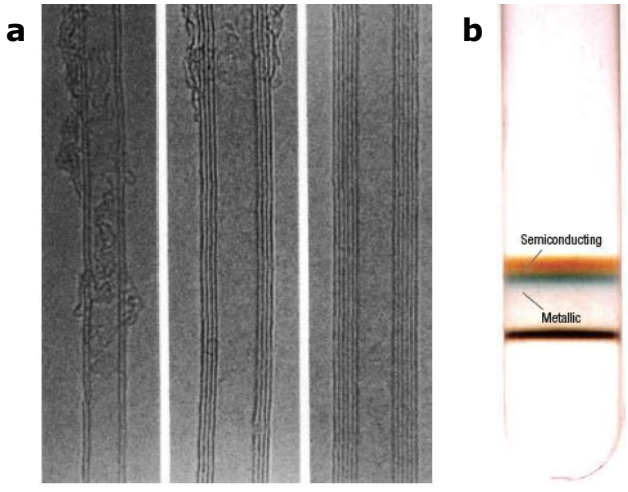

Figure 2.3: (a) TEM image of CNTs grown using arc discharge method. CNTs in the image show double-walled to multi-walled nanotubes. Amorphous carbon residue can be seen depending on the pressure of He in the chamber [8]. **(b)** Photograph of CNTs separated by electronic type [9].

2.2.2 CNT Film Preparation and Transfer

For the three different films, we use a dry transfer and a wet transfer technique to suspend the SWNT films across the metal contacts. Aerosol CVD SWNT films have a low adhesion to the nitrocellulose filters due to the direct deposition onto the filter. As a result, we can use a dry press transfer by cutting the films to size and pressing the films CNT side down across the contacts and removing the filter.

For the NanoIntegris CNTs, we have HiPco CNTs in powder and sorted 90% semiconducting tubes in a solution. The sorted CNTs can be directly filtered using vacuum filtration through a 25 nm pore nitrocellulose membrane. To remove any surfactants, we filter water and isopropyl alcohol to clean the nanotubes. The HiPco tubes, which are in powder form, must first be dispersed in a 2% w/v sodium dodecyl sulfate (SDS) solution using a horn sonicator. The tubes are then deposited onto the filter using vacuum filtration. To transfer the films from solution processed films, the CNT film on filter must first be cut to an appropriate size. Next we dissolve the filter in an acetone bath. To suspend the film, we use the platform to gently scoop the CNT film out of the acetone.

2.3 Measurements and Characterization

Thermal measurements were done using the QFI IR scope while biasing the sample with a Keithley 2612 SourceMeter as shown in Figure 2.4. Temperature hysteresis measurements were done from 25 °C to 100 °C on the Peltier stage of the IR scope. The film was held at a bias of 0.5 V for 100 seconds at 25 °C and at 30 °C – 100 °C in 10 °C increments. Resistances steadily decreased as temperature increased. We found very little resistance change when the temperature was swept back to 25 °C. The temperature hysteresis

measurements also help to current anneal the film, which we can verify by resistance stability post anneal.

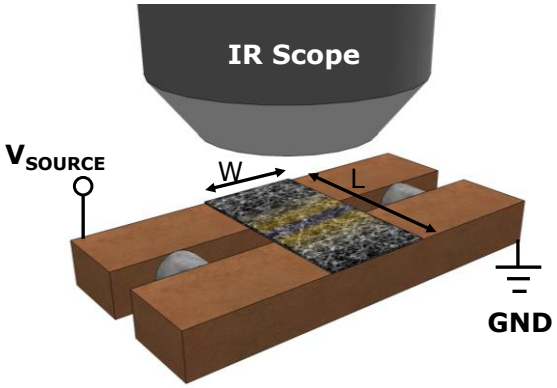

Figure 2.4: A schematic of the experimental setup. The SWNT film is suspended across two contacts and Joule heated under the IR scope.

We use an IR measurement technique that has been used to study thermal transport in several previous works [10-12]. For the IR measurements, we must first calibrate the IR scope. In order to reduce noise from the ambient environment, the stage is held between 70 °C to 90 °C. For all the experiments in this thesis, we use a background temperature of 80 °C. The IR scope does an emissivity calculation of all the materials in the field of view using a reference radiance calibration as shown in Figure 2.5a. Next we take a background temperature of the device under no bias (Figure 2.5b). After calibrations are complete, we can turn on the power in the device and map the temperature profile of the film. The IR scope can capture temperatures with a temperature resolution of 0.1 K and a temporal resolution of 0.1 s. The spatial resolution of the scope depends on the microscope objective. Since the CNT films in this study were on the scale of millimeters, we only used the 1x objective which has a spatial resolution of 36 μm. We use a finite element analysis of a 1D heat

transfer model to extract the thermal conductivity from the temperature profiles obtained by the scope. This is discussed in more detail in Chapter 3.

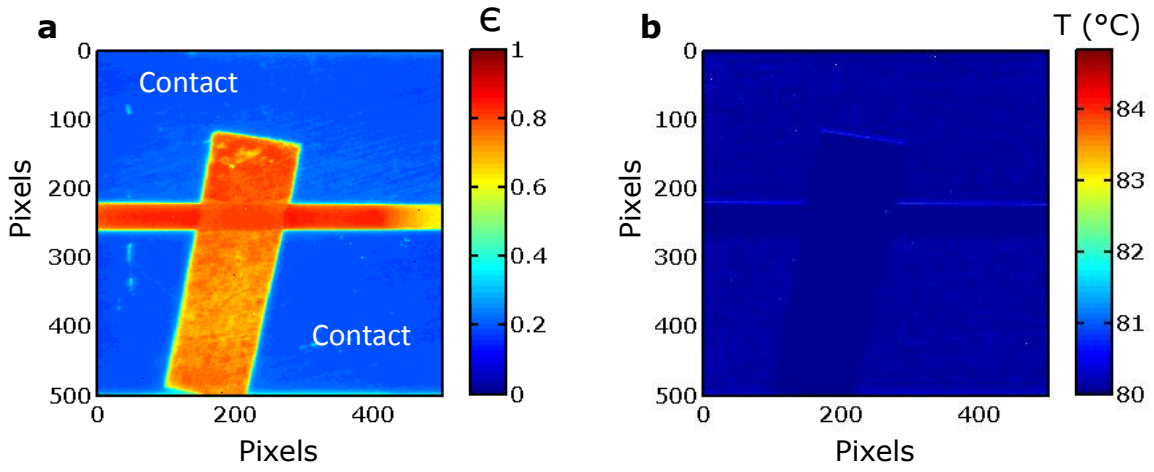

Figure 2.5: (a) Reference radiance map of the device. The CNT film has a higher emissivity than the Pd surface of the contacts. **(b)** Background temperature of the film under no bias. There is no heating and the background temperature is uniformly 80 ^{o}C.

After thermal and electrical measurements of the films were complete, we used a scanning electron microscope (SEM) to measure the device dimensions including the gap length and the width of the film. Next, we used Raman analysis to identify the radial breathing modes (RBM) that were present in the SWNTs of the network. RBMs allow us to extract the diameters of the SWNTs in the film. We found that there were active RBMs in HiPco random CNT film, but none in the aerosol CVD CNT film or the sorted CNT film (Figure 2.6a-d). There is a significant silicon peak around 520 cm^{-1} in the aerosol CVD SWNT that is not present in the other two samples since the film is much thinner which does not completely suppress the Si peak. The vacuum filtration films are about 8 – 16 times thicker, therefore we do not see a significant Si peak. The RBMs in the HiPco random film gave us diameters ranging from 0.83 nm – 0.916 nm.

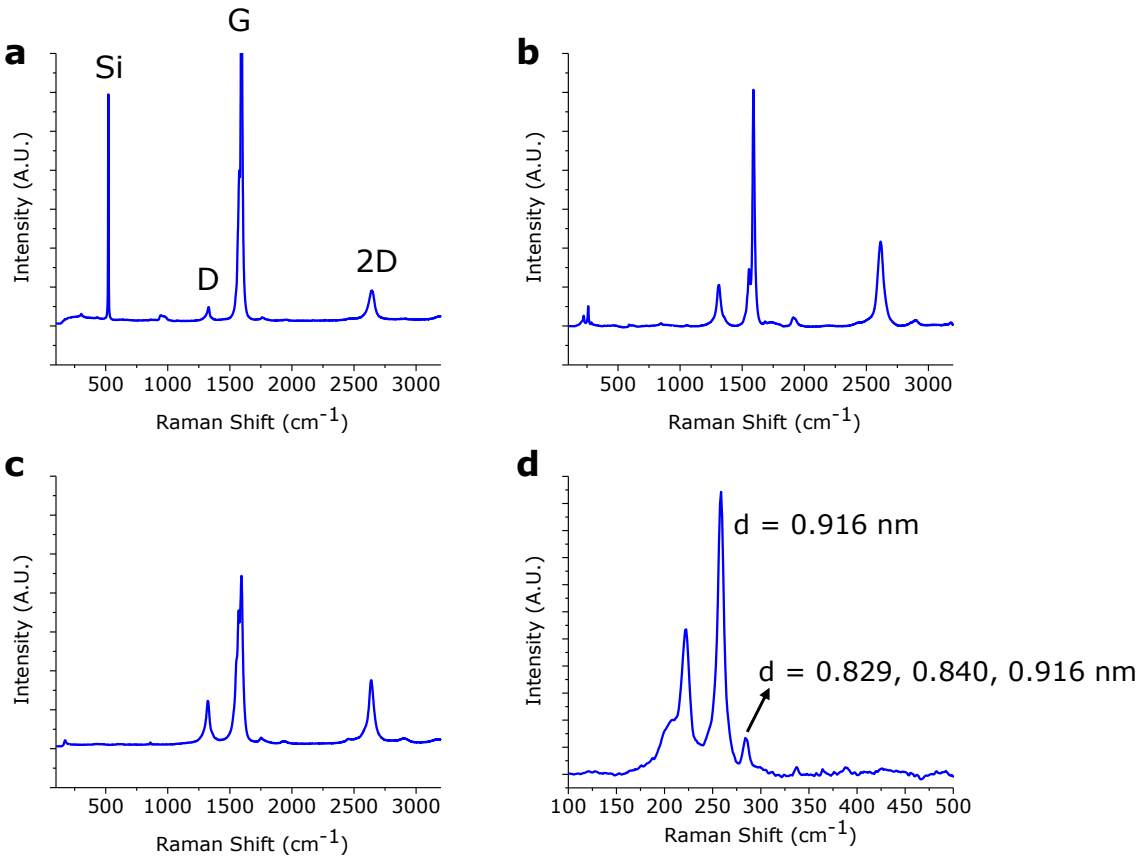

Figure 2.6: Raman analysis of SWNT films on Si substrate using a 633 nm wavelength laser. **(a)** Raman spectrum for Aerosol CVD SWNT film on Si substrate. There is a significant silicon peak since the film thickness is only 50 nm. **(b)** Raman spectrum for HiPco random CNT film. **(c)** Raman spectrum of sorted 90% semiconducting CNTs. **(d)** RBMs of HiPco random CNT film showing CNT diameters ranging from 0.829 nm – 0.916 nm.

2.4 References

[1] B. C. St-Antoine, D. Menard, and R. Martel, "Single-walled carbon nanotube thermopile for broadband light detection," *Nano Letters,* vol. 11, pp. 609-613, 2011.

[2] A. Javey, J. Guo, Q. Wang, M. Lundstrom, and H. Dai, "Ballistic carbon nanotube field-effect transistors," *Nature,* vol. 424, pp. 654-657, 2003.

[3] D. Mann, A. Javey, J. Kong, Q. Wang, and H. Dai, "Ballistic transport in metallic nanotubes with reliable Pd ohmic contacts," *Nano Letters,* vol. 3, pp. 1541-1544, 2003.

[4] A. Moisala, A. G. Nasibulin, D. P. Brown, H. Jiang, L. Khriachtchev, and E. I. Kauppinen, "Single-walled carbon nanotube synthesis using ferrocene and iron pentacarbonyl in a laminar flow reactor," *Chemical Engineering Science,* vol. 61, pp. 4393-4402, 2006.

[5] A. Kaskela, A. G. Nasibulin, M. Y. Timmermans, B. Aitchison, A. Papadimitratos, Y. Tian, et al., "Aerosol-synthesized SWCNT networks with tunable conductivity and transparency by a dry transfer technique," *Nano Letters,* vol. 10, pp. 4349-4355, 2010.

[6] A. G. Nasibulin, A. Kaskela, K. Mustonen, A. S. Anisimov, V. Ruiz, S. Kivisto, et al., "Multifunctional free-standing single-walled carbon nanotube films," *ACS Nano,* vol. 5, pp. 3214-3221, 2011.

[7] M. J. Bronikowski, P. A. Willis, D. T. Colbert, K. A. Smith, and R. E. Smalley, "Gas-phase production of carbon single-walled nanotubes from carbon monoxide via the HiPco process: A parametric study," *Journal of Vacuum Science & Technology A,* vol. 19, pp. 1800-1805, 2001.

[8] T. W. Ebbesen and P. M. Ajayan, "Large-scale synthesis of carbon nanotubes," *Nature,* vol. 358, pp. 220-222, 1992.

[9] M. S. Arnold, A. A. Green, J. F. Hulvat, S. I. Stupp, and M. C. Hersam, "Sorting carbon nanotubes by electronic structure using density differentiation," *Nature Nanotechnology,* vol. 1, pp. 60-65, 2006.

[10] A. Behnam, V. K. Sangwan, X. Zhong, F. Lian, D. Estrada, D. Jariwala, et al., "High-field transport and thermal reliability of sorted carbon nanotube network devices," *ACS Nano*, vol. 7, pp. 482-490, 2013.

[11] D. Estrada and E. Pop, "Imaging dissipation and hot spots in carbon nanotube network transistors," *Applied Physics Letters*, vol. 98, p. 073102, 2011.

[12] M. H. Bae, Z. Y. Ong, D. Estrada, and E. Pop, "Imaging, simulation, and electrostatic control of power dissipation in graphene devices," *Nano Letters*, vol. 10, pp. 4787-4793, 2010.

3. Description of Research Results

3.1 Thermal Conductivity and Contact Resistance Analysis

3.1.1 Thermal Analysis

To extract the thermal conductivity of the sample, we model a one-dimensional (1D) heat transfer equation using finite element analysis [1]. The 1D model is applicable because the sample is suspended, therefore confining heat flow in the one dimension as shown in Figure 3.1b. The model is fitted to experimental temperature profiles to obtain the thermal conductivity and the thermal conductance at the contacts. Since the thermal measurements are done in air and under bias, we must account for heat loss due to convection (h_{conv}), heat loss due to radiation (h_{rad}), the input power (p'), and heat conduction across the sample [2]. Figure 3.1 shows the device schematics.

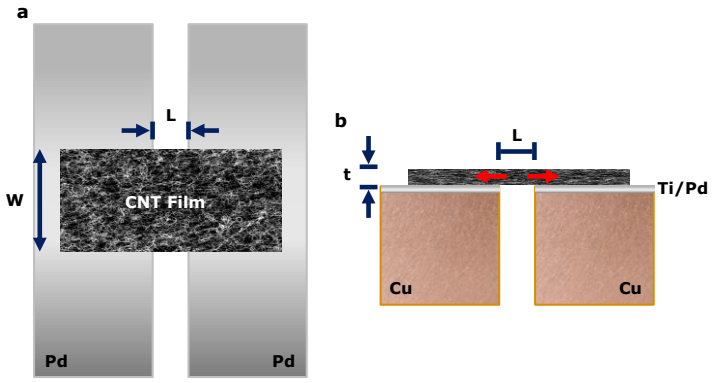

Figure 3.1: (a) Top-down view of the SWNT film suspended across Pd-coated contacts. (b) Cross-sectional view of SWNT film. Heat flow is shown by the red arrows on the sample. Within the suspended region of the film, heat flow is confined to one dimension. The contacts thermally anchor the sample so that the boundary conditions at the contacts are isothermal.

At steady state, the 1D heat transfer equation is given by:

$$A\nabla\left(\kappa\nabla T\right)+p'-g\left(T-T_0\right)=0 \qquad (3.1)$$

where $A = Wt$ is the cross-sectional area of the film, κ is the thermal conductivity of the film, p' is the power across the film, g is the heat loss coefficient, and T_0 is the ambient temperature. Since the film is suspended across two large contacts that thermally ground the sample, the heat loss at the contacts is different from the heat loss in the suspended region of the film. In the suspended film, the heat loss due to convection and radiation at a single point along the sample is given by:

$$g_{film}\left(T - T_0\right) = A_{surf} h_{conv}\left(T - T_0\right) + \epsilon \sigma_B A_{surf}\left(T^4 - T_0^4\right) \tag{3.2}$$

where ϵ is the emissivity of the film, σ_B is the Stefan-Boltzmann constant, and $A_{surf} = WL$ is the surface area of the film. Since the temperature of film varies with position along the film, we must calculate the heat loss coefficient at each point along the sample. We can linearize the radiative heat loss and estimate the overall g_{film} between the suspended film and the environment:

$$g_{film} = 2Wh_{conv} + 2W\epsilon\sigma_B\left[\left(T^2 + T_0^2\right)\left(T + T_0\right)\right] \tag{3.3}$$

where W is the width of the film. For the supported film on the contact, the heat loss coefficient $g_{contact}$ is extracted from fitting to the temperature profile. The contact quality varies depending on the sample since there is a thermal and electrical contact resistance between the film and the metal. The thermal contact resistance is estimated by $g_{contact}$ whereas the electrical contact resistance is measured and extracted using the transfer length method (TLM) [3]. We take into account the contact resistance using

$$p' = I^2(R_{film} - R_C)/L \tag{3.4}$$

where R_C is the resistance between the sample and the contact for both contacts, R_{film} is the resistance of the suspended film, and L is the length. For our model, we assume that the

thermal conductivity of the film is constant along the film and the power is uniformly distributed across the film.

3.1.2 Transfer Length Method

When current flows from the contact to a semiconductor, most of that current is transferred within a transfer length (L_T) [3]. The transfer length is defined as:

$$L_T = \sqrt{\rho_C / R_{sh}} \tag{3.5}$$

where ρ_C is the specific contact resistivity and R_{sh} is the sheet resistance of the semiconductor. We can model the total resistance for two terminal devices as:

$$R_T = \frac{R_{sh}}{W} L + 2R_C \tag{3.6}$$

To extract the electrical contact resistance, films were suspended across three test structures with varied gap lengths as shown in Figure 3.2. Film dimensions were varied across the structures due to the wet transfer process. To account for dimension discrepancies, TLM extractions accounted for the sample width:

$$R_T W = R_{sh} L + 2R_C W \tag{3.7}$$

Since L_T is generally around 1 μm for graphene devices which is much smaller than the actual contact length, we can exclude the contact length from our TLM normalization [4].

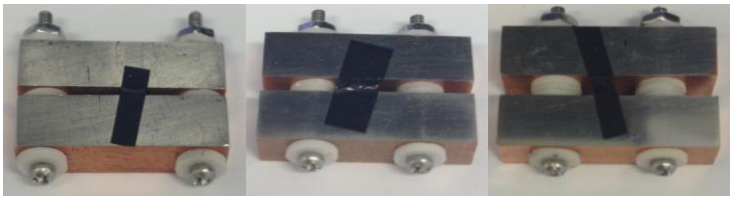

Figure 3.2: SWNT films suspended across Cu/Ti/Pd contacts. Device 1, 2, and 3 have one, two, and three washers separating the contacts respectively. Contact resistance is extracted using TLM from the three different film lengths.

3.2 Experimental Results

For this study, we measured the thermal conductivity of three different films: aerosol CVD grown SWNT films (Figure 3.3a), HiPco random SWNT networks (Figure 3.3b), and 90% metallic SWNT networks (Figure 3.3c).

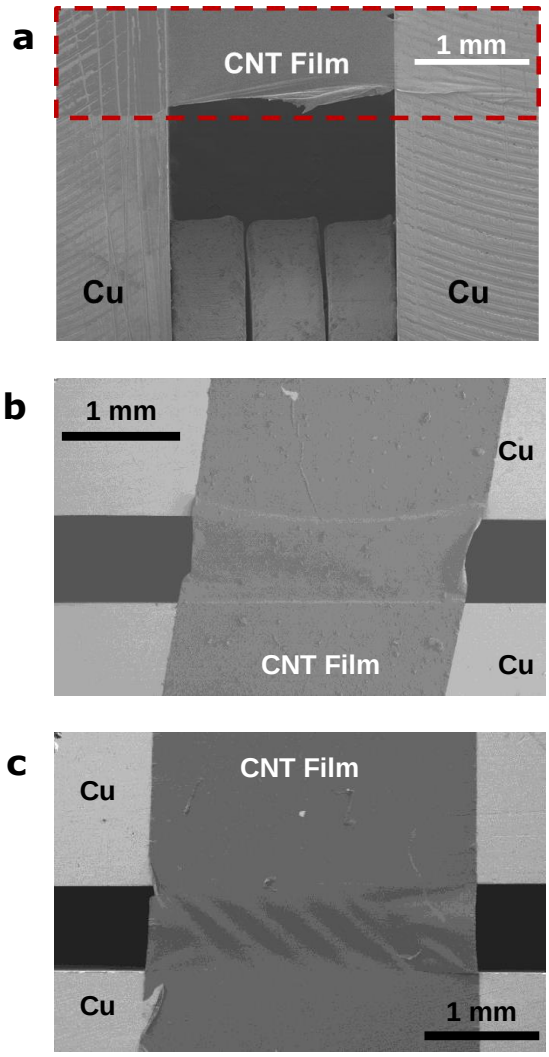

Figure 3.3: SEM image of SWNT films suspended across thermometry platform. **(a)** Aerosol CVD SWNT film suspended using dry transfer. **(b)** Solution processed HiPco random SWNT film suspended across Cu/Ti/Pd contacts. **(c)** 90% semiconducting SWNT film suspended across contacts.

3.2.1 TLM Results

The aerosol CVD SWNT films were transferred onto the platforms using a dry, press transfer method [5]. The SWNT film adheres to the thermometry platform through Van der Waals forces. To improve the adhesion to the contacts, we used contacts with higher surface roughness. As shown in Figure 3.4, the contact resistivity between the SWNT film and the Cu was approximately 2 kΩ·mm. Since the SWNT film is not a perfectly smooth surface, the large contact surface roughness greatly increased contact resistance. This resulted in the majority of the power dissipated by the contacts rather than across the suspended film. However, since the contacts were large compared to the film, there was no significant heating at the contacts.

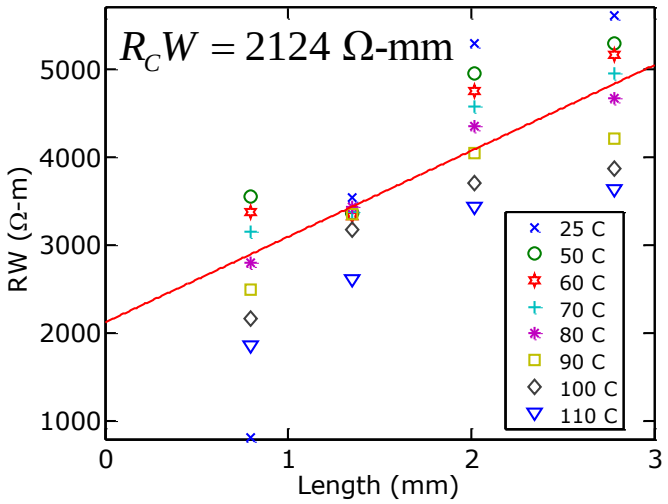

Figure 3.4: Resistance normalized by width as a function of the sample length. For aerosol CVD SWNT films, the contact resistance is higher due to the rough contacts and the low SWNT density in the film.

For the solution processed HiPco random SWNT networks, we transferred films onto three platforms with different gap lengths as shown in Figure 3.3. The overall resistance of the films was much lower due to the increase in film thickness as well as density of the film. The contacts were electrochemically polished and coated with 150 nm Ti and 150 nm Pd to

improve both contact area and contact resistance. Using TLM, we extracted a contact resistivity of approximately 50 Ω·mm for the unsorted tubes (Figure 3.5a). For the 90% semiconducting tubes which were also solution processed, we found the contact resistivity to be 0.7 Ω·mm (Figure 3.5b).

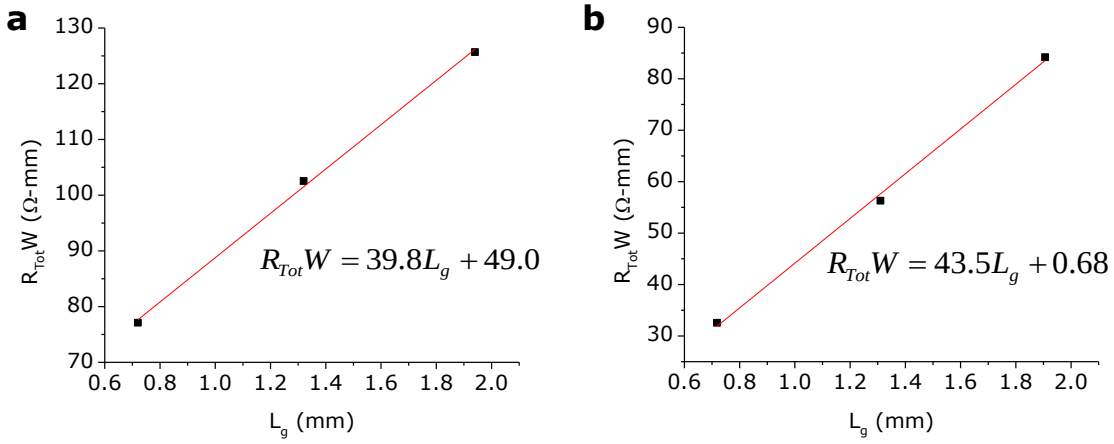

Figure 3.5: (a) The TLM extraction of the HiPco random SWNT film gives a normalized contact resistance of approximately 50 Ω·mm. **(b)** For the 90% semiconducting SWNT film, the normalized contact resistance was much lower at about 0.7 Ω·mm.

3.2.2 *Thermal Analysis Results*

To extract the thermal conductivity, we use the temperature profile captured by the IR scope to create an averaged one dimensional temperature profile. An averaged thermal profile reduces background noise from measurements (Figure 3.6a-d).

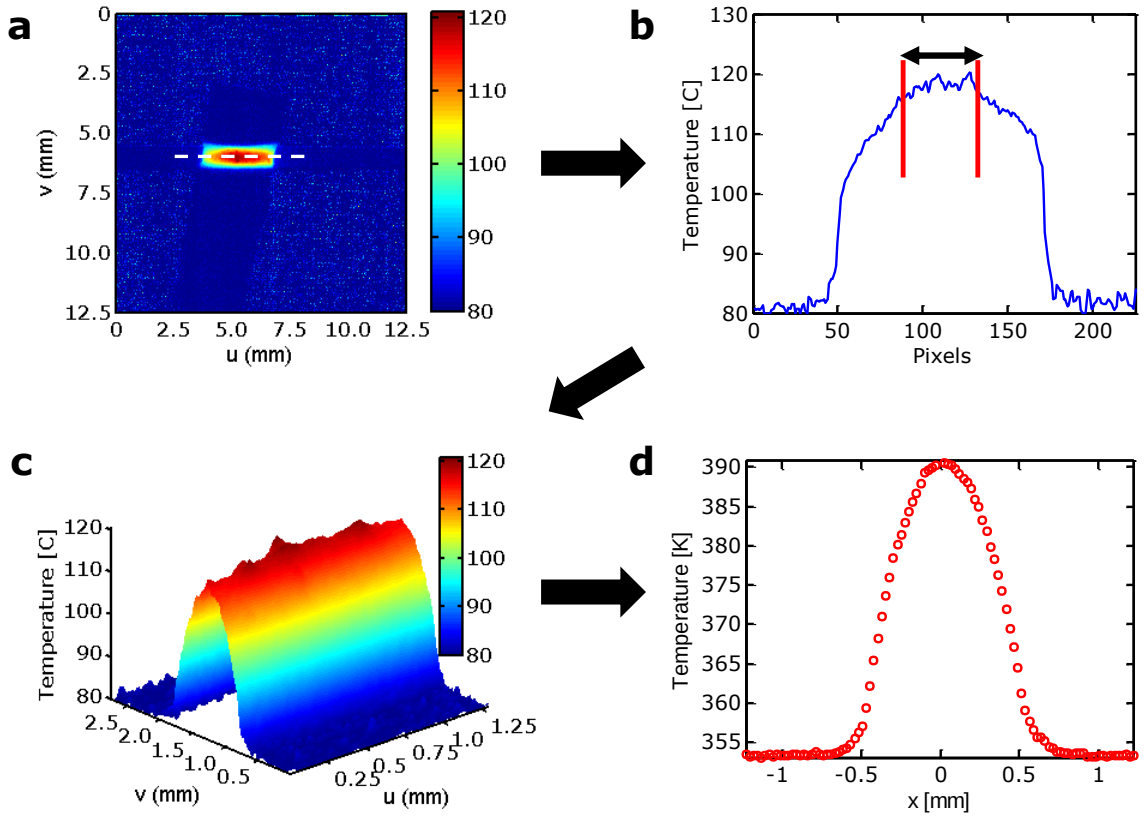

Figure 3.6: Temperature profile extraction from raw IR measurements. **(a)** Averaged temperature profile of the sample while under bias. **(b)** Cross-sectional cut in u-axis, shown by the white dashed line, was used to determine the best window of temperatures to take an average. **(c)** Temperature profile of the film over the averaged window. **(d)** Average temperature profile of device excluding edge effects. Contact noise is eliminated and the temperature profile is smooth.

Due to the folding in the SWNT film at the edge shown in Figure 3.7, we exclude the edges from our thermal analysis. From SEM, we measure the dimensions of the film to be L = 1.35 mm and W = 5.66 mm. Using atomic force microscopy, we estimate the thickness of the film to be ~200 nm. However, using absorbance measurements as demonstrated by

Nasibulin et al., we find the SWNT film to be ~50 nm thick [6]. Since there was no distinct edge in the AFM measurement, we use the thickness obtained from the absorbance measurements for the extraction. From the averaged thermal profile, we fit our model to the temperature profile and extract a thermal conductivity of ~140 $Wm^{-1}K^{-1}$ (Figure 3.8a-b).

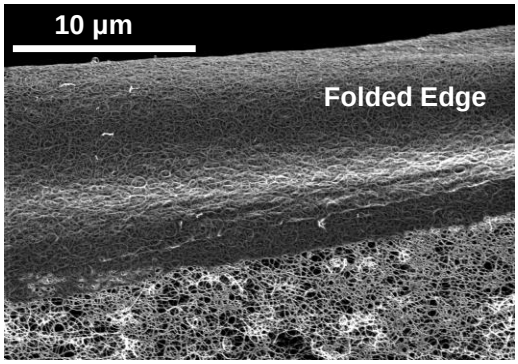

Figure 3.7: SEM image of a suspended aerosol CVD SWNT film at the edge of the film. The folded region shows a greater SWNT density.

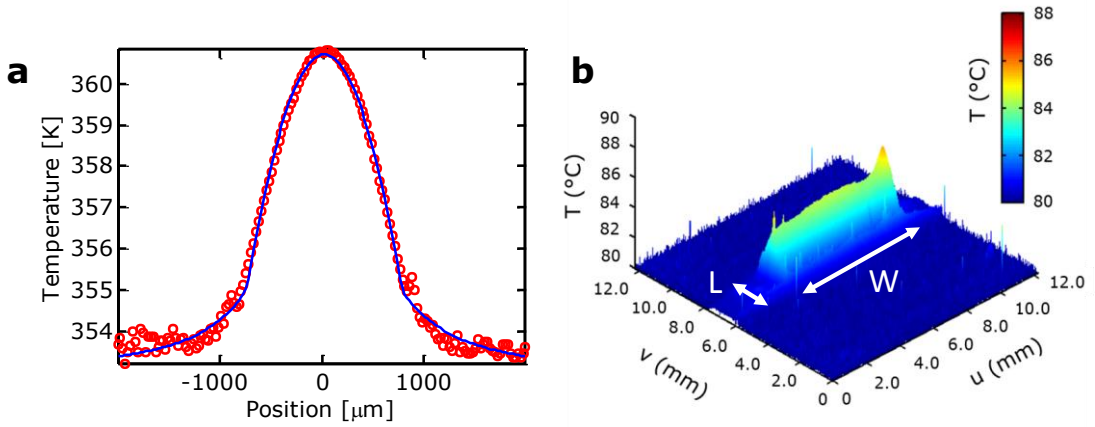

Figure 3.8: (a) Red dots represent the temperature data acquired by the IR Scope. Blue line is the fitted line from the model. **(b)** Raw IR image of the aerosol CVD film under bias. The edge of the film shows significant heating compared to the rest of the film.

In the HiPco random SWNT films, we noticed hot spots in the center of the film due to catalyst particles as shown in Figure 3.9a-b. The film had dimensions of W = 2.46 mm and L = 0.93 mm. The height of the film, measured using a profilometer, was found to be about 330 – 450 nm. Overall we extract the thermal conductivity to be ~40 $Wm^{-1}K^{-1}$for the

HiPco film (Figure 3.10a-b). Due to the increase in film density, we noticed a greater temperature increase in the film as shown in Figure 3.10b.

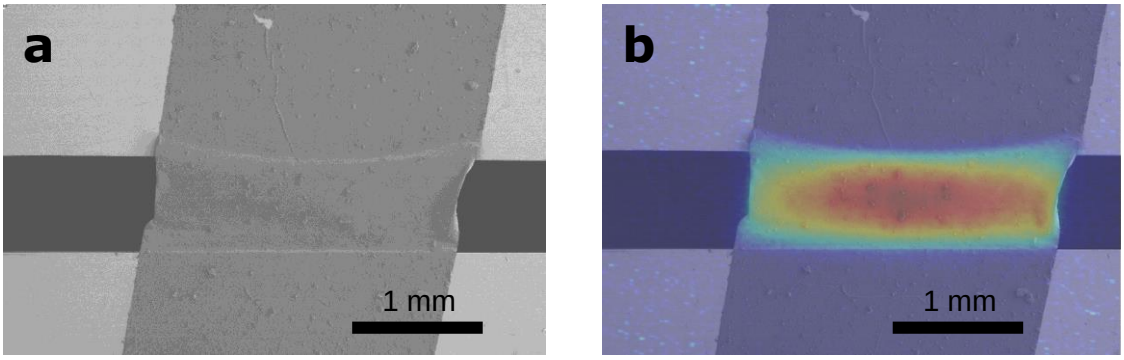

Figure 3.9: (a) SEM image of HiPco film suspended across contacts. **(b)** Overlay of temperature profile obtained from IR scope. Hotspots are prominent at catalyst particle locations.

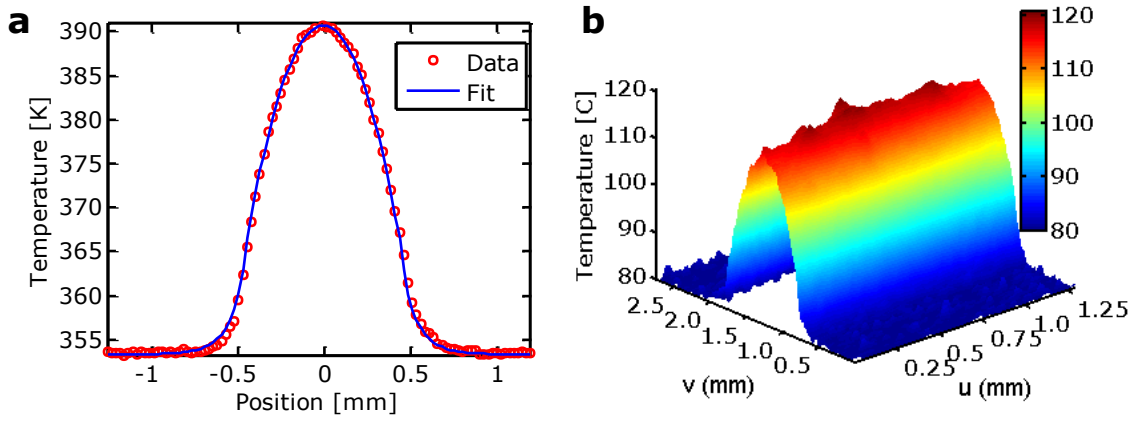

Figure 3.10: Thermal imaging of HiPco random SWNT films. **(a)** Fitting of the thermal model to the average temperature profile. **(b)** Raw thermal IR image of the HiPco random film under bias. The catalyst particles on the surface of the film result in hotspots.

Next, we studied the thermal properties of a film with 90% semiconducting nanotubes. The films were sorted using density gradient ultracentrifugation and purchased through NanoIntegris [7]. The SWNT go through a purification process to remove large catalyst particles and then dispersed in a surfactant for separation. The film dimensions were

W = 2.46 mm and L = 0.72 mm. The height of the film was approximately 780 – 870 nm. By fitting the temperature profile, we extracted a thermal conductivity of ~110 $Wm^{-1}K^{-1}$ (Figure 3.11a). We also note that the SWNT film had much more uniform heating due to similar junction type and purity (Figure 3.11b).

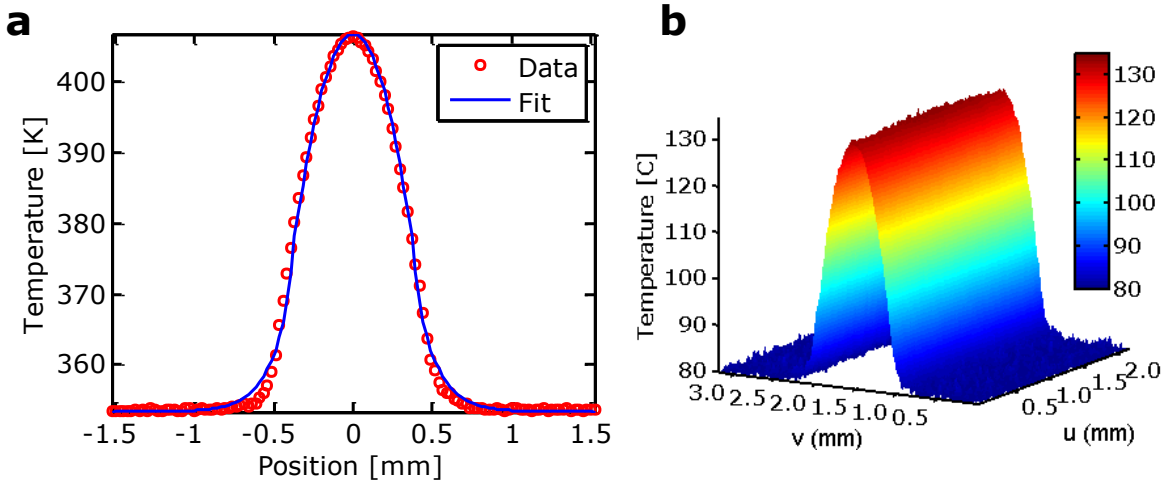

Figure 3.11: Thermal imaging of 90% semiconducting SWNT films. **(a)** Fitting of the thermal model to the average temperature profile. **(b)** Raw IR image of the 90% semiconducting film under bias. The temperature profile is much more uniform because the junctions in the film are mostly semiconducting – semiconducting junctions which have similar thermal resistances.

3.3 References

[1] E. Pop, D. A. Mann, K. E. Goodson, and H. Dai, "Electrical and thermal transport in metallic single-wall carbon nanotubes on insulating substrates," *Journal of Applied Physics*, vol. 101, p. 093710, 2007.

[2] F. P. Incropera, D. P. DeWitt, T. L. Bergman, and A. S. Lavine, *Fundamentals of Heat and Mass Transfer*, 6th ed. Hoboken, NJ: John Wiley & Sons, Inc., 2007.

[3] D. K. Schroder, *Semiconductor Material and Device Characterization*, 3rd ed. Hoboken, NJ: John Wiley & Sons, Inc., 2006.

[4] K. L. Grosse, M. H. Bae, F. F. Lian, E. Pop, and W. P. King, "Nanoscale joule heating, Peltier cooling and current crowding at graphene-metal contacts," *Nature Nanotechnology*, vol. 6, pp. 287-290, 2011.

[5] A. Kaskela, A. G. Nasibulin, M. Y. Timmermans, B. Aitchison, A. Papadimitratos, Y. Tian, et al., "Aerosol-synthesized SWCNT networks with tunable conductivity and transparency by a dry transfer technique," *Nano Letters*, vol. 10, pp. 4349-4355, 2010.

[6] A. G. Nasibulin, A. Kaskela, K. Mustonen, A. S. Anisimov, V. Ruiz, S. Kivisto, et al., "Multifunctional free-standing single-walled carbon nanotube films," *ACS Nano*, vol. 5, pp. 3214-3221, 2011.

[7] M. S. Arnold, A. A. Green, J. F. Hulvat, S. I. Stupp, and M. C. Hersam, "Sorting carbon nanotubes by electronic structure using density differentiation," *Nature Nanotechnology*, vol. 1, pp. 60-65, 2006.

4. Conclusion

4.1 Summary and Discussion

In summary, this study has simultaneously examined the thermal and electrical transport properties of suspended SWNT films using IR thermometry on devices under voltage bias. The approach using IR thermometry allows for rapid thermal analysis with minimal lithography and sample preparation. This method can be applied to any electrically conductive film that can be Joule heated to temperature rise of at least 0.2 K. Our study of SWNT films reveals that nanotube network morphology such as volume density and chirality affect the thermal conductivity of the overall network.

The thermal conductivities we extract from our temperature profiles are in essence an average thermal conductivity of the entire film. Since the temperature profile along the sample is non-uniform, the κ at each point along the sample may be different if the film has a large temperature gradient and if the thermal conductivity has a dependence on temperature. We also note that the extracted thermal conductivity is dependent on knowledge of the thickness of the film, therefore uniform film thickness and accurate thickness measurements are crucial to the thermal conductivity extraction. Our results are in good agreement with previous studies of thermal conductivity of SWNT networks [1, 2]. The aerosol CVD SWNT films had a much lower thermal conductivity due to the lower SWNT density. The solution-processed SWNTs films had a higher SWNT density as well as greater film thickness. At high power, the resistance of the film steadily increased in both the forward and reverse sweeps, suggesting the nanotubes within the SWNT film were breaking down. For the 90%-semiconducting film, the resistance increased much more rapidly. We believe this is due to

the fact that there was no gate to turn on the semiconducting tubes in the measurement, therefore leading to breakdown at lower power.

4.2 Future Work

In order to compare the thermal conductivities of the different films studied in this work, we must fabricate films of equal mass density and thickness. Solution processing offers the best control for mass density. The Volkov and Zhigilei study on the effect of mass density and nanotube length on thermal conductivity as shown in Figure 4.1, gives an expression for thermal conductivity of a network as:

$$\kappa = \frac{\kappa_0}{1 + \mathrm{Bi}_T / 12} \tag{4.1}$$

where κ_0 is the thermal conductivity of the network assuming that thermal conductivity of individual nanotubes is infinite [3]. Bi_T is the Biot number of each individual nanotube which is a measure of the distribution of temperature in the nanotube and is given as:

$$\mathrm{Bi}_T = \frac{\sigma_c \langle N_J \rangle L_T}{\kappa_T A_T} \tag{4.2}$$

The Biot number depends on the average number of junctions on the nanotube ($\langle N_J \rangle$), the junction conductance (σ_c), length of the nanotube (L_T), cross-sectional area of the nanotube (A_T) and the thermal conductivity of each individual nanotube (κ_T). As nanotube length L_T becomes infinitely large, the thermal conductivity becomes independent of nanotube length and linearly proportional to mass density (ρ). Thermal conductivity approaches an asymptotic value of $\kappa^{\infty} = (1/3)(A_T / (\pi R_T^2))\kappa_T \phi$ where A_T is the cross-sectional area, R_T is the radius, and

κ_T is the thermal conductivity of an individual nanotube in the network (Figure 4.1). The volume fraction of the nanotubes is given by $\phi = \pi R_T^2 L_T n_V$, where n_V is the volume number density of nanotubes. In order to explore the effect of nanotube mass density and length on thermal transport, we will employ our measurement technique to extract the thermal conductivity of the networks while tuning the network parameters such as density, nanotube junction type, and nanotube length and diameter.

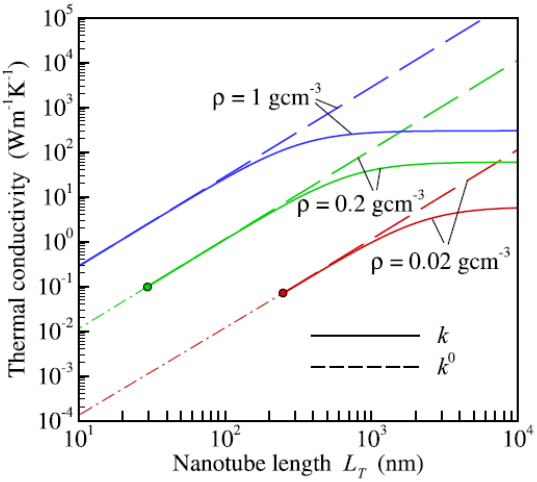

Figure 4.1: Thermal conductivity as a function of nanotube length for various mass densities and nanotube lengths. Thermal conductivity is linearly proportional to mass density. It is also shown that beyond 1 μm, the effect of nanotube length plateaus at constant mass density [3].

4.3 References

[1] M. E. Itkis, F. Borondics, A. Yu, and R. C. Haddon, "Thermal conductivity measurements of semitransparent single-walled carbon nanotube films by a bolometric technique," *Nano Letters,* vol. 7, pp. 900-904, 2007.

[2] J. Hone, M. Whitney, C. Piskoti, and A. Zettl, "Thermal conductivity of single-walled carbon nanotubes," *Physical Review B,* vol. 59, pp. 2514-2516, 1999.

[3] A. N. Volkov and L. V. Zhigilei, "Heat conduction in carbon nanotube materials: Strong effect of intrinsic thermal conductivity of carbon nanotubes," *Applied Physics Letters,* vol. 101, p. 043113, 2012.